PAN

Opto-Electronics Review

journal homepage: https://journals.pan.pl/opelre

Self-noise reduction in a FOG-based rotational seismometer confirmed by Allan variance analysis

Piotr Zając[1]*, Piotr Amrozik[1], Rafał Kiełbik[1], Cezary Maj[1], Michał Szermer[1], Łukasz Starzak[1], Bartosz Pękosławski[1], Grzegorz Jabłoński[1], Wojciech Tylman[1], Anna Kurzych[2,3], Leszek R. Jaroszewicz[2,3]

[1] Department of Microelectronics and Computer Science, Lodz University of Technology, ul. Wolczanska 221, 93-005 Lodz, Poland
[2] Institute of Applied Physics, Military University of Technology, ul. gen. Sylwestra Kaliskiego 2, 00-908 Warsaw, Poland
[3] Elproma Elektronika Sp. z o.o., ul. Dunska 2A, 05-152 Czosnow, Poland

Article info:

Article history:
Received 02 Aug. 2024
Received in revised form 05 Nov. 2024
Accepted 05 Nov. 2024
Available on-line dd Nov. 2024

Keywords:
fibre-optic rotational seismometer;
fibre-optic gyroscope;
Allan variance;
noise;
angle random walk;
bias instability.

Abstract

Reducing noise in fibre-optic gyroscope (FOG)-based rotational seismometers is crucial in guaranteeing their applicability as future high-precision sensors. This paper presents a practical approach to noise analysis of a designed and manufactured FOG-based three-axis rotational seismometer. The performed measurements show that proper identification of noise sources and subsequent changes to the device's configuration which addressed these noise issues, visibly improved the Allan deviation plot of the device. In particular, angle random walk was reduced from 100–200 to around 35 nrad/s/$\sqrt{\text{Hz}}$ and bias instability – from several dozens down to single nrad/s. These improvements were achieved only by elimination or mitigation of the impact of all noise sources, without changing any optoelectronic components of the constructed device and without applying any additional post-processing methods.

1. Introduction

The technology of fibre-optic gyroscope (FOG) [1] has been well-known for over forty years, and steady advances in the field have made it one of the most promising solutions for rotation sensors. They are widely used in navigation systems [2,3], especially in space [4] and submarine [5] applications, as well as in seismology [6] and structural health monitoring [7]. FOGs are based on the Sagnac effect [8,9] which induces a phase shift between two counter-propagating light beams when their optical path is rotated. Due to its intrinsic way of operation, it has many advantages: high sensitivity, relatively small size and cost, wide measuring range, high reliability, and insensitivity to linear motion. Moreover, due to its inherent reciprocity and the use of a low-coherence amplified spontaneous emission (ASE) source, the FOG interferometer does not suffer from the noise caused by the Kerr effect, back-scattering, or polarisation coupling [10]. FOG performance exceeds that of competitive technologies such as ring laser gyroscopes [11, 12]. Therefore, FOGs are considered the most promising solution for future high-sensitivity gyroscopes.

More than 45 years after its first publication [13], the FOG is now the most important and technically developed implementation of the Sagnac fibre-optic interferometer. However, it is not the only one. Fibre-optic rotational seismometers (FORSs) for the so-called rotational seismology [14], including the blueSeis-3A and blueSeis-1C (iXblue, France) [15], and FOSREM-3D (Elproma Elektronika Ltd, Poland) [16], are also appearing on the market. These systems should be considered FOG-based in that they use the so-called minimum FOG configuration [17] in their optical parts and closed-loop technology solutions in their electronic parts. However, besides the above-mentioned similarity to FOGs, it is important to note the fundamental differences between these solutions. A FOG measures angle change around each axis, while a FORS measures angular velocity. Hence, a FORS directly measures the phase shift due to the Sagnac effect, while a FOG integrates it over time. This means that the integration drift of the measurement is one of the main issues in FOGs, while it does not exist in FORSs [6]. In addition, size reduction often becomes a fundamental requirement for FOGs while not for FORSs, which allows the latter to use sensor loops with larger dimensions, leading to higher sensitivities. However, FORSs pose other challenges: they should be able to operate continuously over

*corresponding author at: piotr.zajac@p.lodz.pl

https://doi.org/10.24425/opelre.2024.152766
1896-3757/ Association of Polish Electrical Engineers (SEP) and Polish Academic of Sciences (PAS). Published by PAS

months or even years, have internal power source, and, in some cases, use renewable energy power sources, efficiently transfer extremely large amounts of data, and be remotely configurable [18].

Nevertheless, the analysis of noise sources and an effective noise reduction to increase FOG-based systems sensitivity is a widely recognised challenge. While in theory, it should be quite easy to reduce the noise floor in such systems just by improving the parameters of their optoelectronic components, this naïve approach does not yield the expected results in practice. During the realisation of the FOSREM project [16], it was observed that the measured noise floor of the manufactured FORS was an order of magnitude higher than the one predicted by the theoretical model used. Subsequently, several additional noise sources (e.g. variable temperature gradients caused by air circulation inside the enclosure) were found to degrade the noise performance of the FORS that had not been taken into account in theoretical analyses. These issues needed to be addressed first to ensure that the device was able to achieve its optimum theoretical noise performance.

Therefore, this work tackles the problem of noise from the practical perspective of improving noise performance when measuring rotation. The underlying analysis, shown in the next sections, is based on the following scheme. First, a general summary of major noise sources in a FOG-based system is presented in section 2 together with a method of their investigation based on Allan variance. Next, the structure of the tested FORS is briefly described in section 3. Finally, in section 4, starting from the initially measured amplitude spectral density, Allan deviation curves are compared with the expected, ideal characteristics to identify frequency ranges where the noise performance can be improved. Device modifications that can potentially bring this improvement are also listed in this part of the paper. In subsections 4.1 to 4.5, the implementation of these changes is presented together with measurements performed to evaluate their effect. The process of measurements and improvements is iteratively repeated. In the end, a conclusion is formulated on how a particular device parameter influences the noise performance indicators obtained using the Allan variance analysis.

2. Noise sources and their analysis by the Allan deviation method in a FOG-based system

The noise in a FOG depends on a multitude of factors, related to both optical and electronic sources. The following formula describes the theoretical value of total noise in a FOG [19]:

$$ARW = \frac{\lambda c}{\sqrt{2}\pi D L}\sqrt{N_T^2 + N_C^2 + N_S^2 + N_{RIN}^2}\,, \qquad (1)$$

where ARW denotes the angle random walk, λ is the wavelength, c is the speed of light in vacuum, D and L denote the diameter and the length of the fibre loop, respectively, N_T is the thermal noise of the preamplifier, N_C is the dark current noise, N_S is the photon shot noise and N_{RIN} is the relative intensity noise (RIN) of the light source. The latter four are given by:

$$N_T^2 = \frac{4k_BT}{R\eta^2P^2}, \qquad N_C^2 = \frac{ei_D}{\eta^2P^2}$$
$$N_S^2 = \frac{e}{\eta P}, \qquad N_{RIN}^2 = \frac{\lambda^2}{4c\Delta\lambda} \qquad (2)$$

where k_B is the Boltzmann constant, T is the temperature, R is the feedback resistance of the transimpedance amplifier, η is the photodetector responsivity, P is the incident light power on the detector, e is the electron charge, i_D is the photodetector dark current and $\Delta\lambda$ is the spectral width of the light source, defined as full-width at half-maximum (FWHM).

Consequently, noise sources are: the avalanche photodiode (APD) dark current noise and the thermal noise of the transimpedance preamplifier in the electronic circuit (which converts the optical signal into an electrical one), and, mainly the photon shot noise and the RIN of the light source in the optical circuit. Among these, the RIN was found to be often the dominant contributor [20]. However, some possible noise sources are not included in (1), so the real noise performance will be worse. In addition, some FOG parameters such as transimpedance amplifier feedback resistance or light source coherence time are fixed in hardware and cannot be easily changed after device production to improve the noise performance. Therefore, this paper presents a practical approach to reducing noise in a FOG-based seismometer based on understanding the origins of all noise effects, followed by optimisation of noise-related device parameters, but without replacing any optical or electronic components of the device.

Numerous attempts have been reported in the literature to reduce the noise of FOGs. Researchers have suggested modifying the design by hardware improvements [21, 22], real-time filtering [23, 24], predictive algorithms [25], discrete wavelet transforms [26] or even neural networks [27]. Instead, this paper focuses on identifying, analysing, and optimising those system parameters which are configurable and allow reducing noise after the device has already been manufactured.

The Allan variance (or Allan deviation) plot method is widely used to describe the noise performance of FOGs. It was initially invented for calculating the stability of oscillators [28]. It was later discovered that it can be effectively applied for identifying noise effects in inertial sensors [29], in particular ring laser gyroscopes [30]. It has become a standard for testing FOGs [31] and is widely used by researchers in noise analysis to estimate FOG accuracy [32–35].

The Allan variance analysis is a method of characterising data sequences in the time domain. If a random measurement signal of a gyroscope, $\Omega(t)$, is averaged over some time interval τ yielding a series of averaged values, then Allan variance $\mathrm{AV}(\tau)$ is defined as half the mean value of the squares of the differences between successive averaged values. Its square root, called the Allan deviation (AD), is also used [36], which represents the standard deviation of frequency fluctuations as a function of τ.

A typical AD log-log plot for a FOG-based rotational sensor is shown in Fig. 1. The y-axis is scaled in the same units as the measured signal (rad/s instead of deg/h typically used for FOGs), while the x-axis shows the averaging period τ.

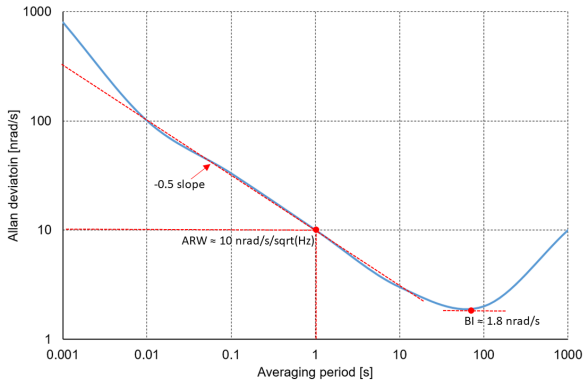

Fig. 1. Typical AD plot for a FOG-based rotational sensor, showing only the ARW and BI parameters calculation for clarity.

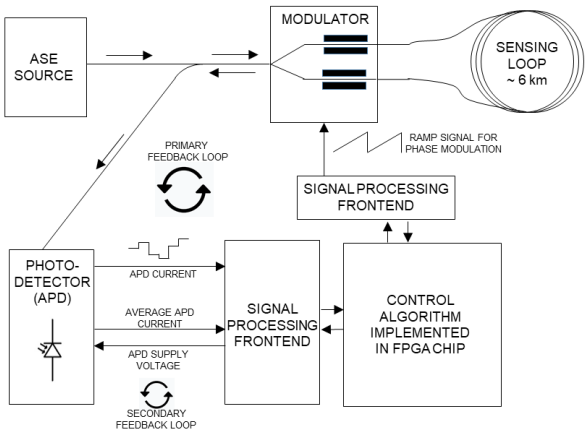

Fig. 2. Simplified block diagram of the analysed FOG-based rotational seismometer.

For a signal sampled at some frequency f_s, the lower bound of data points on the x-axis is $\tau_{min} = 1/f_s$. There are five different noise components which can be identified in an AD plot: quantisation noise, rate random walk, rate ramp, ARW, and bias instability (BI). Among them, the last two are of a particular interest for describing the performance of FOG-based sensors [19, 37] and have been commonly used to classify FOGs by grade [1, 38]. An AD plot typically includes a –0.5 slope section due to the presence of white noise in the signal. The y-value of this slope at $\tau = 1$ s determines the ARW value in rad/s/$\sqrt{\text{Hz}}$ (or rad/$\sqrt{\text{s}}$). Thus, when ARW is decreased, the noise floor is lowered and the FOG performance is improved. The minimum of the AD plot represents the BI (in rad/s), which represents the long-term stability of the measured signal.

3. FOG-based rotational sensor

Figure 2 presents a simplified block diagram of the designed and manufactured FOSREM-3D fibre-optic rotational seismometer which employs a well-known FOG structure. For clarity, it only shows the subsystem for one of the three axes of the device. FOSREM-3D comprises three such independent single-axis subsystems. For a more exhaustive description of this measurement system, see [39, 40].

The primary feedback loop shown in Fig. 2 is the most important part of the entire closed-loop system. The light is generated by an ASE module. Such light sources generally provide higher optical output power than the more commonly used superluminescent light emitting diode (SLED) ones. Consequently, just a single ASE is sufficient to supply all the three axes through a 1×3 fibre-optic coupler. In each axis, the light beam is split into two counter-propagating waves which enter a sensing loop from opposite directions. Avalanche photodiode is used as a photodetector, which in general provides higher sensitivity than PIN diodes, at the expense of its increased noise figure.

These two waves interfere and produce optical power proportional to the raised cosine of their phase difference $P(\Delta\phi)$, subsequently converted to current by an APD. As the derivative of the cosine function is zero for $\Delta\phi = 0$, the sensitivity of the sensor would be very low if this principle were applied directly. In addition, it would not be possible to identify the direction of rotation. In order to increase sensitivity and to disambiguate the direction of rotation, operation with a certain bias is desired. The bias is introduced by phase modulation using a multi-functional integrated optical chip (MIOC), applying a voltage-controlled phase shift to the light wave both before entering and after exiting the fibre loop. The MIOC also performs splitting and coupling of the light beam. The phase of each wave is modulated twice, before entering the sensing loop and after leaving this loop. If the modulation were constant, both waves would experience the same phase shift. Therefore, the modulator shifts the phase alternately in two directions with the half-period equal to the group delay of the loop (square-wave modulation). Then the system effectively works in two bias points located at the same level on opposite sides of the raised cosine function. Thus, if there is no rotation, the light waves interference induces a constant current at the APD. Any rotation of the fibre loop causes a phase shift which makes the output of the APD produce an error signal, in the form of a square wave with two different current levels being generated during different modulation steps. The difference between these levels is proportional to the rotation rate (see Fig. 3.7 in Ref. [11]). In a closed-loop operation, to compensate for rotation, a linear ramp, whose slope is proportional to the rotation rate, is added to the modulation signal. Note that due to the limited range of the modulator, the ramp needs to be reset by subtracting or adding a multiple of 2π to the phase shift, see chapter 8 in Ref. [11] for details. Based on the known slope and loop parameters, it is then possible to calculate the rotation rate that produced the measured error signal.

The system is additionally equipped with a secondary feedback loop that keeps the average APD current at a constant level. After measuring the averaged current (at a low frequency to eliminate the impact of the modulation), the control algorithm increases or decreases the APD bias voltage to appropriately adjust the APD current.

The manufactured three-axis FOSREM-3D device is shown in Fig. 3. The dissipated power and the resulting temperature were found to be of vital importance for noise in the system. Therefore, to ease the understanding of temperature effects inside the case, a drawing that shows how particular parts are positioned has also been provided. Each

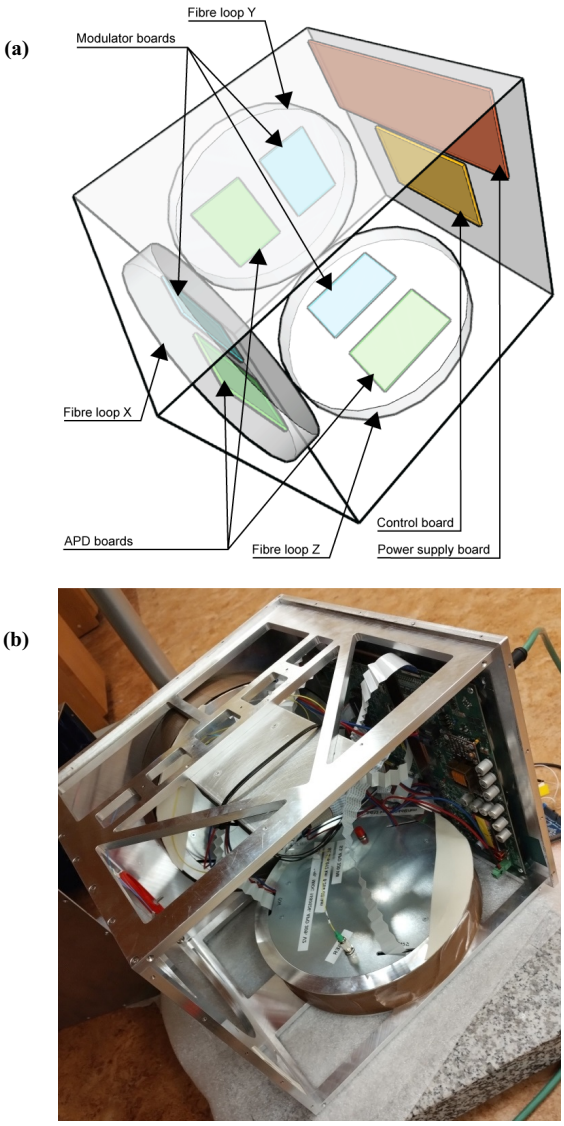

Fig. 3. Internal structure of most important components of FOSREM-3D (a). Photograph of FOSREM-3D with open case, with two out of three fibre loops mounted (b).

fibre optic loop is wound on a cylindrical metal body, each of them being mounted on a different wall of the enclosure so that they are positioned perpendicularly to each other. Each cylinder has an APD and a modulator board connected to its fibre loop. Additionally, the power supply and control boards are fixed to the fourth enclosure wall. The ASE light source module is mounted on the fifth wall. All system components are connected to one another with ribbon cables. Table 1 shows the approximate power consumption by every module.

Table 1.
Power consumption by FOSREM-3D.

Module	Power consumption
Power supply board	3 W
Control board	10 W
APD board	3×1 W = 3 W
Modulator board	3×3 W = 9 W
Total	**25 W**

4. Identification and mitigation of noise sources

The lower limit of a rotational seismometer resolution is determined by the so-called self-noise which is the sensor output signal when the sensor is at rest and there is no rotational motion at the input. Estimating this limit, therefore requires a recording of the output signal from a seismically quiet time interval with a background level of ground motion lower than the sensor self-noise level. Self-noise is difficult to measure, especially in laboratories located in urban environments. Hence, it is customary to use overnight recordings [41]. Although noise is usually characterised by a power spectral density (PSD), the FOSREM-3D self-noise will be reported as an amplitude spectral density (ASD) which is the square root of PSD. The main reason for this approach is the possibility of directly comparing ASD to the measured rotation rate and, consequently, analysing AD instead of AV.

Figure 4 presents an example of a baseline ASD obtained with FOSREM-3D together with the corresponding AD plot (Fig. 4). These measurements were performed in a laboratory at the Lodz University of Technology, Poland with the aim of investigating the self-noise of the device. As it can be seen, the raw ASD [the blue line in Fig. 4(a)] is "fluctuating" with an amplitude increasing with frequency. For this reason, frequency spectra were smoothed by averaging every 100 data points. The result is presented by the orange line in Fig. 4(a).

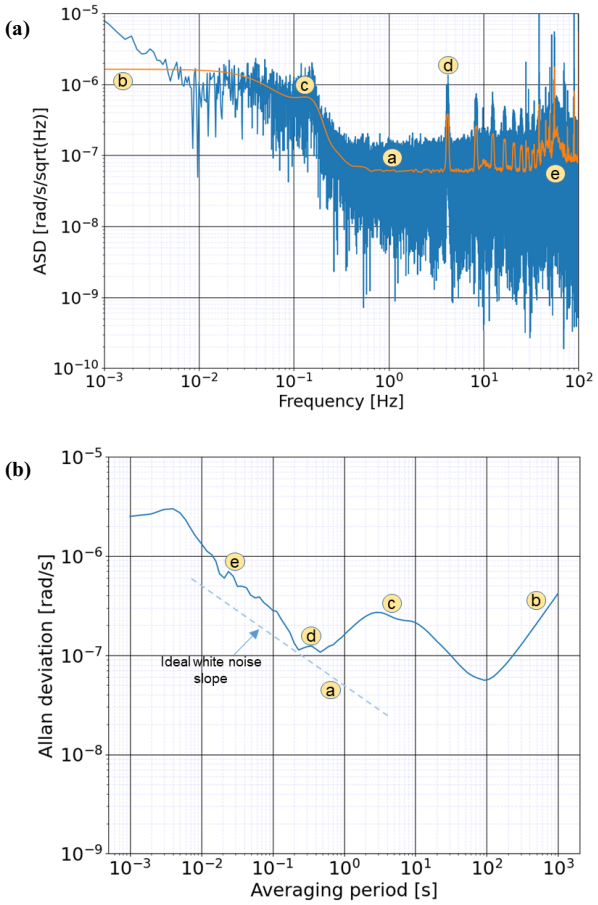

Fig. 4. Sample ASD (a) and the corresponding AD (b) plots. See the text for a description of the marked regions.

Based on the obtained characteristics, several kinds of noise or disturbances observed at the FOSREM-3D output have been identified (see Fig. 4):

(a) white noise, in the entire frequency spectrum,
(b) slow drift of rotation rate (with a time constant of the order of hours),
(c) noise "bump" in the frequency range between 0.01 Hz and 2 Hz,
(d) 2π resets of the ramp, causing noise peaks at the corresponding frequencies,
(e) interference from devices powered from the 50 Hz grid.

The next five subsections discuss methods for eliminating or mitigating the above noise types.

4.1. Reduction of white noise

Several FOSREM-3D parameters that affect white noise can be changed "on-the-fly" in its software. They include:

- the ASE source power (which determines the input optical power for the sensing loop),
- the APD bias voltage (which determines the APD responsivity, i.e., the optical power to current conversion ratio),
- the synchronicity parameter which allows the buffer window used for calculating averaged samples of the APD output to be shifted in time.

The light source used is a mini-broadband ASE [42] whose output power can be changed with a resolution of 1 dB, up to a maximum of 16 dBm. A single source is used for all three axes. Since the attenuation is approximately 15 dB in each axis, the maximum power per axis at the end of its fibre loop is around 420 µW. This power is then converted into electrical current by the APD. Unsurprisingly, it was found during investigations that higher light source power results in lower noise (Fig. 5). In particular, for low power, the AD curve is relatively flat below $\tau = 1$ and gets progressively steeper as power is increased, which decreases ARW. For instance, changing the power from 4 dBm to 13 dBm allowed ARW to be reduced from 90 nrad/s/$\sqrt{\text{Hz}}$ to 58 nrad/s/$\sqrt{\text{Hz}}$. However, it was also discovered that starting from the power of around 13 dBm, no further improvement in ARW is achieved.

Another way to boost the output signal strength is to increase the APD responsivity (measured in A/W) by raising its bias voltage. The APD used has a breakdown voltage of 38.6 V and the closer the bias voltage is to this value, the stronger the avalanche multiplication effect and the higher current induced for a given optical power. Thanks to dedicated hardware, FOSREM-3D allows the APD bias voltage to be set in a wide range with a high resolution. The AD curves obtained for four values of APD bias are shown in Fig. 6. The effect is similar to the one of increasing the light source power, though considerably weaker. Increasing the APD responsivity allows ARW to be reduced, but only up to a certain point. In particular, increasing the APD bias voltage from 29.6 V to 35.9 V resulted in a reduction of ARW of about 7 nrad/s/$\sqrt{\text{Hz}}$. However, a further increase of this voltage had little to no effect.

The synchronicity parameter shifts the time window over which the circuit gathers samples before they are averaged and processed by the control algorithm. The idea is shown in Fig. 7: the signal is continuously sampled by an analogue-to-digital converter (ADC) while the signal value stays roughly at the same level, apart from small fluctuations due to noise. However, due to a change of polarisation in the MIOC element, an unusual peak is observed for one sample in every period of the four-step modulation: the non-instantaneous voltage shift on the MIOC electrodes produces a transient, resulting in the ADC sample wrong value. It is the role of the median filter applied to all buffer samples to eliminate the impact of this wrong sample. Additionally, the buffer window may span two different cycles (see Fig. 7), which may further influence the final rotation rate calculated by the control algorithm. Therefore, measurements were performed to see if the buffer window position impacts the noise. It was found (see Fig. 8) that slightly better results were obtained when the window was so positioned that it

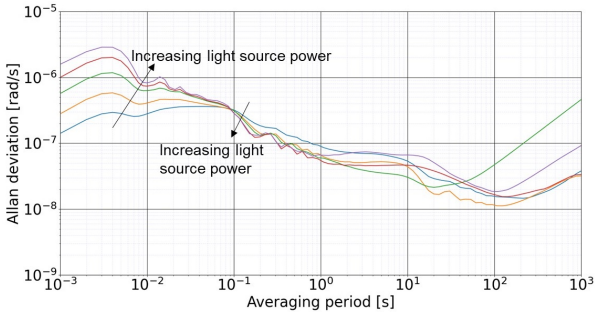

Fig. 5. Impact of light source power (4 dBm, 7 dBm, 10 dBm, 13 dBm, and 16 dBm) on FOSREM-3D self-noise represented in an AD plot.

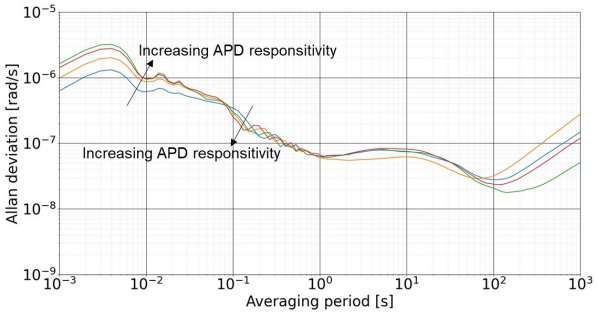

Fig. 6. Impact of APD responsivity (29.6 V, 35.9 V, 37.4 V, and 38.3 V) on FOSREM-3D self-noise represented in an AD plot.

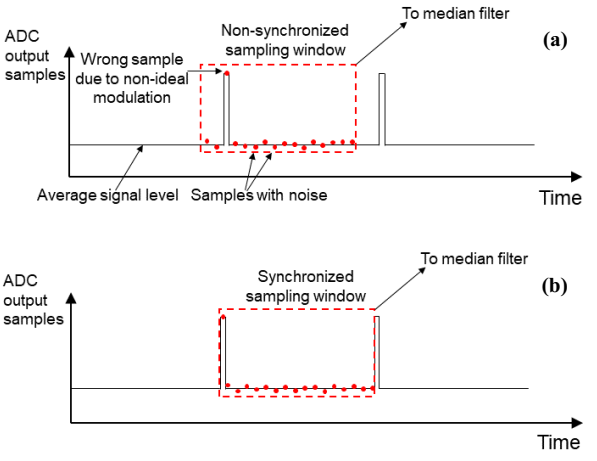

Fig. 7. Non-synchronised (a) and synchronised (b) windowing for the median filter.

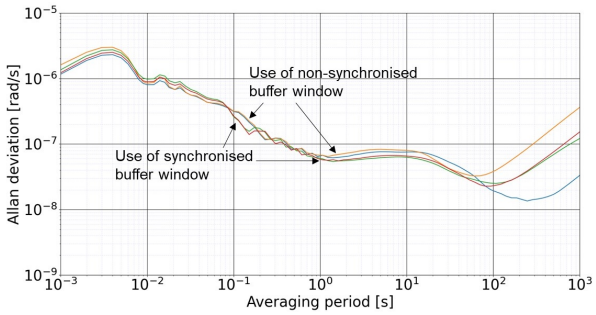

Fig. 8. Impact of median filter window synchronisation on FOSREM-3D self-noise represented in an AD plot.

exactly matched a particular single step of the modulation scheme (i.e., all the samples in the window corresponded to the same modulation step). The average improvement of ARW was around 6 nrad/s/$\sqrt{\text{Hz}}$, which is relatively small, but this change was consistent across multiple tries.

4.2. Mitigation of slow drift

It was observed that the measured rotation rate drifts slowly across time, sometimes even reaching the rate of ±10 µrad/s per hour (the Earth's rotation rate being around 52 µrad/s at the latitude of the testing facility). It was discovered that this drift was caused by two factors.

The first cause of the long-time rotation rate drift are temperature gradients between different parts of the sensing loop. The device has a high heat capacity due to its weight and metal construction, thus it can take several hours for it to thermally stabilise. For example, at least 8 hours are typically required after it is turned on until the temperatures in all its parts reach their steady states. Over this period, different parts are warming up at different speeds, producing thermal gradients between different fragments of the sensing loop and affecting the rotation rate measurement results due to the refraction index being highly dependent on temperature. A similar effect also occurs when the external temperature changes, producing a temperature drift of the output signal. To mitigate the related drift, the device structure was slightly modified by thermally isolating the sensing loops from other components as much as possible to make their temperature more uniform.

The second important factor is the impact of temperature fluctuations inside the device on the parameters of electrical components. In particular, the APD responsivity (which affects the total gain of the readout circuit) was proven to be quite sensitive to temperature. For this reason, a secondary feedback loop has been implemented between the hardware and the algorithm, allowing the APD bias voltage to be regulated to maintain a constant APD current regardless of temperature fluctuations (see Fig. 2). A secondary ADC with a low-pass filter is used to measure the average APD current with a low sampling frequency. Based on these samples, the APD bias voltage is adjusted by a PID controller within the control algorithm so that the current stays at the same predefined level.

After the above improvements were implemented, the drift amplitude and rate decreased considerably. Figure 9 shows a sample output signal (rotation rate) before and after

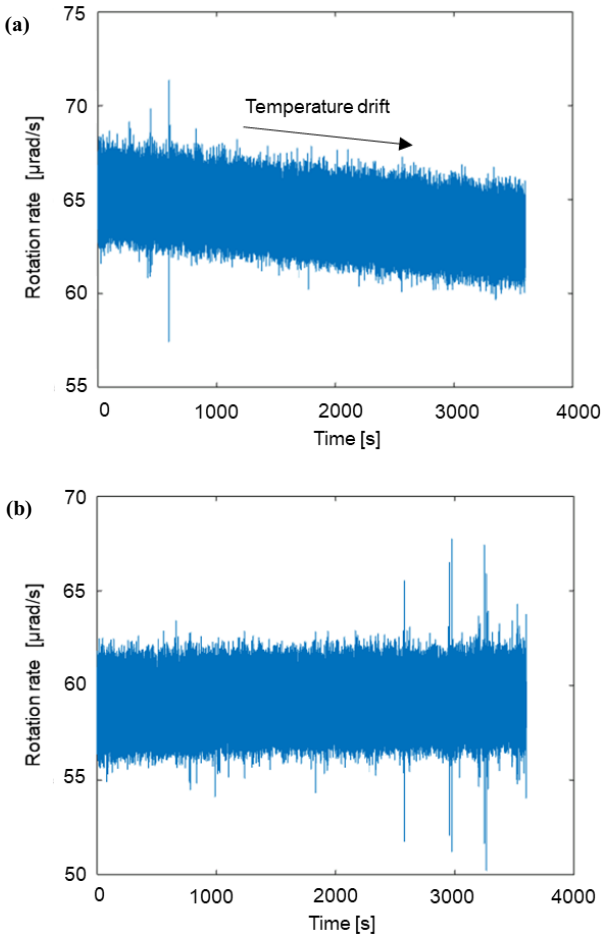

Fig. 9. Rotation rate measurement results obtained over one-hour intervals with a sampling frequency of 1 kSps: original device structure (a) and modified device structure (b).

the device modifications. It must be emphasised, however, that while the temperature drift reduction was a welcomed result, it was observed that this kind of drift did not affect the ARW parameter of FOSREM-3D.

4.3. Elimination of low-frequency noise

As observed in Fig. 5 and 6, there is a visible noise "bump" in the AD curve in the frequency range from 0.01 Hz to 2 Hz. A similar effect was reported by other researchers: see, for example, Fig. 3 in Ref. [43] or Fig. 9 in Ref. [38]. Since this type of noise exists at low frequencies, a temperature-related effect was the most likely candidate for its cause. It was postulated that the air circulation inside the device caused small temperature gradients, producing noise at these frequencies.

To validate the above hypothesis, AD curve measurements were performed with the device enclosure fully closed, as well as after removing three of its side walls and its top wall. The results are presented in Fig. 10. For the open enclosure, the "bump" became clearly larger, which may indicate that the free airflow caused a higher temperature gradient in the fibre loop, translating into higher noise in the frequency range under consideration. To mitigate this effect, the airflow around metal cylinders with fibre loops was restricted. Even a partial restriction of air circulation already improved the results considerably (see the green line

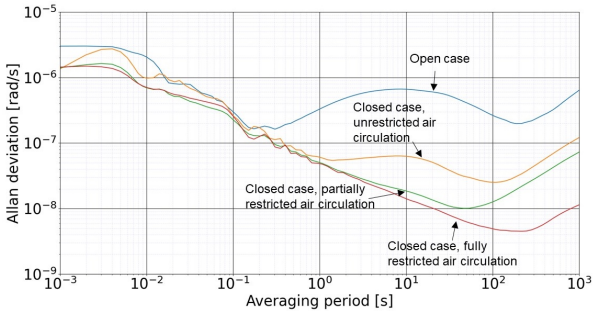

Fig. 10. Impact of air circulation inside the enclosure of FOSREM-3D on its self-noise represented in an AD plot.

in Fig. 10). The best results were obtained when the airflow was restricted completely (see the red line in Fig. 10), with the noise bump in the related frequency range disappearing completely. This enabled a significant reduction of ARW to be achieved, down to only 49 nrad/s/$\sqrt{\text{Hz}}$ and a reduction of BI to only 4.5 nrad/s.

4.4. Reduction of disturbances from ramp resets

During the development of the control algorithm, it was observed that the ASD spectrum contained spikes at around 4 Hz and its harmonics [see Fig. 4 where they are marked as (d)], with exact frequencies different for each FOSREM-3D axis. It was discovered that they were caused by ramp resets. The ramp whose slope is directly proportional to the rotation rate is the feedback signal generated by the control algorithm to compensate the error (please see section 3). Since the slope cannot be infinite due to the limited voltage range, it needs to be periodically reset, which is done by subtracting a voltage $2V_\pi$ corresponding to a 2π phase shift at the MIOC output [see Fig. 11(a)].

In theory, this should not affect the output signal (corresponding to rotation rate), because a 2π shift does not effectively change the phase of the light. However, in practice, the reset is not instantaneous, which affects one or more samples input to the algorithm [see Fig. 11(b)]. Normally, such samples may be filtered out and should not affect the output rotation rate calculated by the algorithm. However, it was discovered that in the output signal after the ramp reset, a short spike is followed by a slow decay [see Fig. 11(c)], which cannot be filtered out in post-processing. This unwanted artefact could be explained by the non-linear dependence of the phase shift $\Delta\phi$ generated by the MIOC on its input voltage, especially in higher temperatures. Consequently, while the MIOC input voltage varies linearly in time, the resulting phase shift of the light wave does not, which contaminates the output signal. This hypothesis was supported by the results of software simulations in which MIOC nonlinearity was artificially introduced and similar tail-like signal was observed at the output.

It is worth noting that the frequency of the resulting noise signal is not constant, but it increases linearly with rotation rate due to more frequent ramp resets. Surprisingly, this noise contribution is also closely related to the temperature drift. To explain this effect, let us consider an example that shows how the noise resulting from ramp resets manifests in each of the following cases:

(1) no temperature-induced rotation rate drift,
(2) temperature-induced rotation rate drift much lower than actual rotation,
(3) temperature-induced rotation rate drift comparable to actual rotation rate.

In the first case, ramp resets will occur with a constant frequency since rotation rate will be mostly stable. Similarly, in the second case, this frequency will be almost constant, albeit a little less than in the first case. Therefore, in the ASD spectrum, a spike will be seen [such as the one in Fig. 12(a)]. Due to how AD is calculated, such a narrow-band noise will have a very small impact on the corresponding AD plot and, consequently, on ARW. Conversely, the frequency of ramp resets will vary significantly in the third case. To understand this effect, suppose the average rotation rate is 2 µrad/s and the relative temperature-induced drift is ±1 µrad/s. The rotation rate will then be drifting between

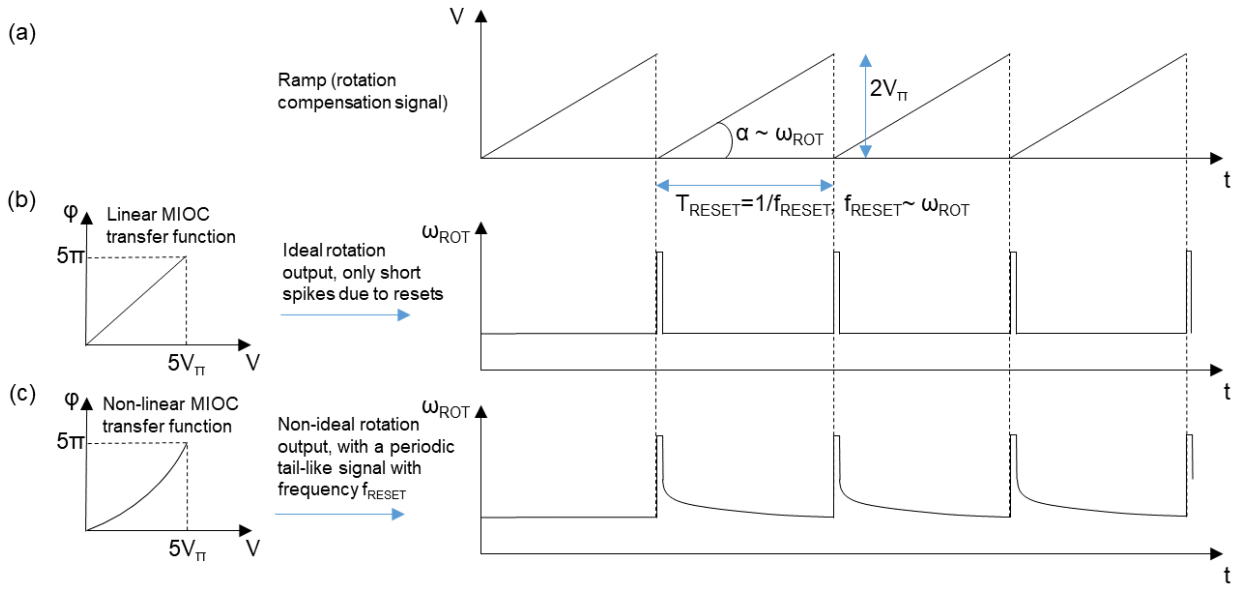

Fig. 11. Impact of ramp resets and MIOC non-linearity on the rotation rate signal: ramp (rotation rate compensation) signal (a), rotation rate output signal for a linear MIOC (b), rotation rate output signal for a non-linear MIOC (c).

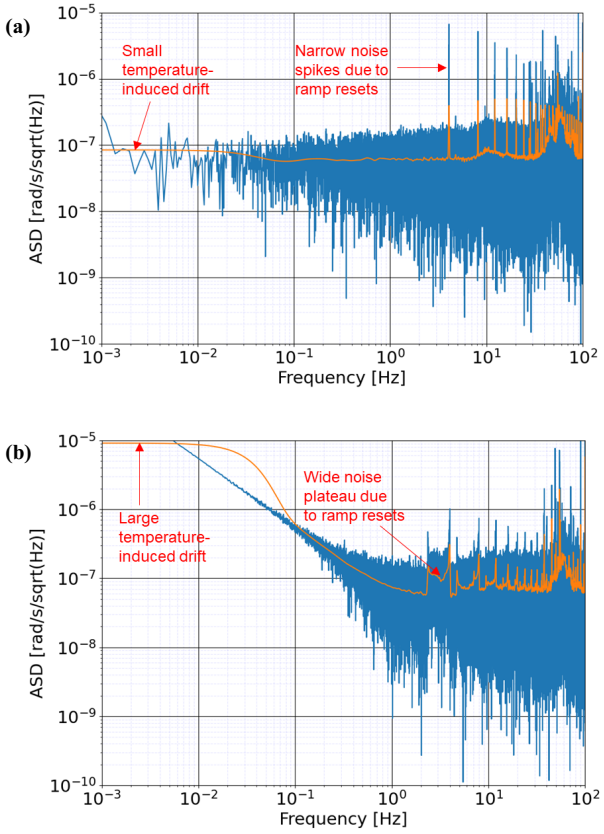

Fig. 12. Impact of ramp resets on the self-noise of FOSREM-3D represented in ASD plots for a small temperature drift (a) and a large temperature drift (b).

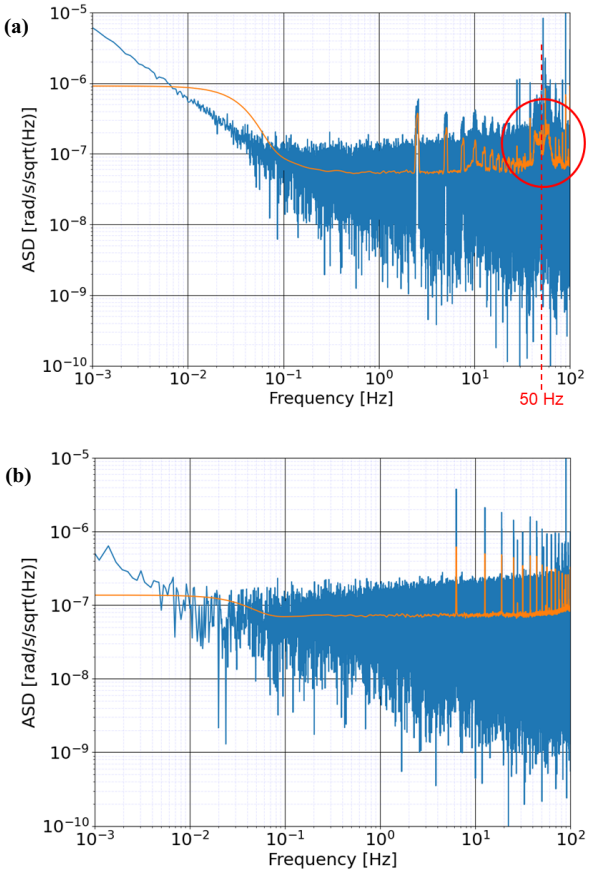

Fig. 13. ASD of the FOSREM-3D output signal: with an off-grid linear power supply operating in the vicinity (a) and after switching this power supply off (b).

1 µrad/s and 3 µrad/s. Consequently, the ramp reset frequency will be varying between f_{reset} and $3f_{reset}$. This will be reflected in the ASD spectrum as a plateau across a relatively wide frequency range [Fig. 12(b)], causing ARW to increase.

Therefore, the method of eliminating the temperature drift described in sub-section 4.3 is also efficient in mitigating the impact of ramp resets on ARW, as the related noise will be contained within a narrow range of frequencies. Admittedly, it solves this problem indirectly and only partially. Fully eliminating the related disturbance at its source is only possible by ensuring a perfect linearity of the MIOC module. Further research into this issue is planned for the future.

4.5. Impact of grid frequency-related disturbances

In Fig. 13(a), one can observe a wide bump around the 50 Hz frequency. It may be caused by either electrical disturbances in the measurement system or by mechanical vibrations caused primarily by nearby devices with transformers powered from a 50 Hz grid. This noise artefact disappeared [Fig. 13(b)] when measurements were performed without any 50 Hz interference sources in the immediate vicinity of FOSREM-3D. It is impractical to prevent this kind of interference by filtering or any kind of post-processing, as the 50 Hz frequency lies inside the intended bandwidth of FOSREM-3D. To ensure that these disturbances do not affect the self-noise measurement, the device should be placed far away from their sources.

4.6. Combined effect of device improvements

The improvements described in sub-sections 4.1 to 4.5 resulted in a much smoother and regular AD plot representing the device self-noise, containing a clear monotonically decreasing section with a –0.5 slope spanning across a wide averaging period range (Fig. 14). At the same time, they allowed ARW to be reduced from between 100 nrad/s/$\sqrt{\text{Hz}}$ and 200 nrad/s/$\sqrt{\text{Hz}}$ to around 35 nrad/s/$\sqrt{\text{Hz}}$, which is by at least half an order of magnitude. An even greater improvement was achieved in BI: from between 50 nrad/s and 60 nrad/s down to 5 nrad/s.

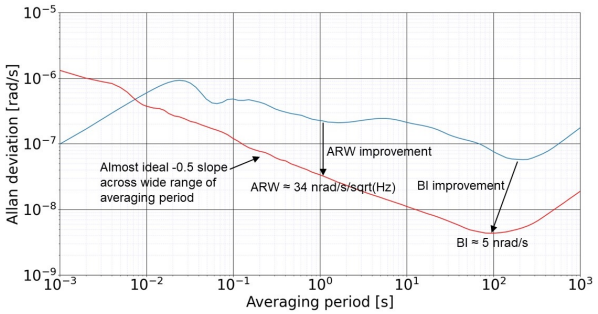

Fig. 14. Sample AD plot of the FOSREM-3D output signal before (blue line) and after (red line) the improvements described in section 4.

5. Conclusions

The results presented in this paper show that a non-ideal configuration of a FOG-based rotational seismometer or its improper thermal design may significantly harm its noise performance. The following important conclusions can be made based on the analysis of the performed measurements and following improvements.

- The most important factor negatively affecting the ARW of the investigated device is the low-frequency noise caused by air circulation inside the case. The best solution to this issue is to prevent or reduce air circulation around the fibre loops.
- To minimise white noise, light source power and APD responsivity should be as high as possible without saturating the electronic readout circuit. That said, it should be emphasised that increasing light source power or APD responsivity has diminishing returns and does not improve noise performance anymore once the signal strength reaches a certain threshold.
- Although the temperature-related long-term drift does not impact ARW directly, it considerably increases it when coupled with the noise due to ramp resets, especially when the measured rotation rate is low. Therefore, it is advisable to keep this drift small by making the temperature of the sensing loops as uniform as possible. Additionally, an APD current-controlling circuit is useful in keeping the APD current stable and further minimising the temperature-related drift.

The analysis presented in this paper has been aimed at improving AD curves of a FOG-based rotational seismometer with a special emphasis on reducing ARW. It has been shown that it is possible to significantly reduce noise in such a device by a careful optimisation of the system parameters based on a good understanding of noise effect origins. This allows a significant improvement of noise performance without replacing any optical or electronic components, or implementing complex post-processing techniques. It should be emphasised that such an optimisation does not preclude applying signal post-processing at a later stage.

Authors' statement

Research concept and design, P.Z., A.K., and L.R.J.; hardware development, P.Z., P.A., G.J., B.P., Ł.S., C.M., M.S., and R.K.; software development, W.T., R.K., G.J., and P.A.; collection and/or assembly of data, P.Z and R.K.; data analysis and interpretation, P.Z. and C.M.; writing the article, P.Z. and Ł.S.; critical revision of the article, P.A., G.J., M.S., L.R.J., and Ł.S.; final approval of article, L.R.J. and W.T.

Acknowledgements

This work was supported by the Polish Agency for Enterprise Development project FENG.01.01-IP.02-1714/23 and the National Centre for Research and Development project POIR.01.01.01-00-1553/20-00.

References

[1] Lefèvre, H. C. The fiber-optic gyroscope: Challenges to become the ultimate rotation-sensing technology. *Opt. Fiber Technol.* **19**, 828–832 (2013). https://doi.org/10.1016/j.yofte.2013.08.007.

[2] Song, N., Xu, X., Zhang, Z., Gao, F. & Wang, X. Advanced interferometric fiber optic gyroscope for inertial sensing: A review. *J. Light. Technol.* **41**, 4023–4034 (2023). https://doi.org/10.1109/JLT.2023.3260839.

[3] Carr, K., Greer, R., May, M. B. & Gift, S. Navy testing of the iXBlue MARINS fiber optic gyroscope (FOG) inertial navigation system (INS). In *2014 IEEE/ION Position, Location and Navigation Symposium - PLANS 2014*, 1392–1408 (IEEE, 2014). https://doi.org/10.1109/PLANS.2014.6851515.

[4] Grifi, D., Senatore, R., Quatraro, E., Verola, M. & Pizzarulli, A. FOG based INS for satellite launcher application. In *2017 DGON Inertial Sensors and Systems (ISS)*, 1–12 (IEEE, 2017). https://doi.org/10.1109/InertialSensors.2017.8171492.

[5] Heckman, D. & Baretela, L. Improved affordability of high precision submarine inertial navigation by insertion of rapidly developing fiber optic gyro technology. In *IEEE 2000. Position Location and Navigation Symposium*, 404–410 (IEEE, 2000). https://doi.org/10.1109/PLANS.2000.838332.

[6] Kurzych, A. *et al.* Fibre-optic Sagnac interferometer in a FOG minimum configuration as instrumental challenge for rotational seismology. *J. Light. Technol.* **36**, 879–884 (2018). https://doi.org/10.1109/JLT.2017.2769136.

[7] Murray-Bergquist, L., Bernauer, F. & Igel, H. Characterization of six-degree-of-freedom sensors for building health monitoring. *Sensors* **21**, 3732 (2021). https://doi.org/10.3390/s21113732.

[8] Sagnac, G. L'éther lumineux démontré par l'effet du vent relatif d'éther dans un interféromètre en rotation uniforme. *Comptes rendus hebdomadaires des séances de l'Académie des sciences* **157**, 708–710 (1913). https://ether-wind.narod.ru/Sagnac_1913_10/Sagnac_1913_10_fr.pdf.

[9] Post, E. J. Sagnac effect. *Rev. Mod. Phys.* **39**, 475–493 (1967). https://doi.org/10.1103/RevModPhys.39.475.

[10] Lloyd, S. W., Digonnet, M. J. F. & Fan, S. Modeling coherent backscattering errors in fiber optic gyroscopes for sources of arbitrary line width. *J. Light. Technol.* **31**, 2070–2078 (2013). https://doi.org/10.1109/JLT.2013.2261283.

[11] Lefèvre, H. *The Fiber-optic Gyroscope*. Artech House optoelectronics library (Artech House, 1993).

[12] Pavlath, G. A. Fiber optic gyros: the vision realized. *Proc. SPIE* **6314**, 63140G (2006). https://doi.org/10.1117/12.683457.

[13] Vali, V. & Shorthill, R. W. Fiber ring interferometer. *Appl. Opt.* **15**, 1099–1100 (1976). https://doi.org/10.1364/AO.15.001099.

[14] Lee, W. H. K., Çelebi, M., Todorovska, M. I. & Igel, H. Introduction to the special issue on rotational seismology and engineering applications. *Bull. Seismol. Soc. Am.* **99**, 945–957 (2009). https://doi.org/10.1785/0120080344.

[15] iXblue. blueSeis-3A : Portable rotational 3-component seismometer absolute & broadband. https://www.ixblue.com/wp-content/uploads/2022/02/blueSeis-datasheet.pdf (2019) (Accessed: 16th June 2024).

[16] Elproma Electronics. FOSREM : Fibre-optic system for rotational events&phenomena monitoring. https://fosrem.eu/?page_id=10 (2023) (Accessed: 16th June 2024).

[17] Ulrich, R. Fiber-optic rotation sensing with low drift. *Opt. Lett.* **5**, 173–175 (1980). https://doi.org/10.1364/OL.5.000173.

[18] Jaroszewicz, L. *et al.* Review of the usefulness of various rotational seismometers with laboratory results of fibre-optic ones tested for engineering applications. *Sensors* **16**, 1–22 (2016). https://doi.org/10.3390/s16122161.

[19] Korkishko, Y. N. *et al.* Highest bias stability fiber-optic gyroscope SRS-5000. In *2017 DGON Inertial Sensors and Systems (ISS)*, 1–23 (IEEE, 2017). https://doi.org/10.1109/InertialSensors.2017.8171490.

[20] Guattari, F., Chouvin, S., Moluçon, C. & Lefèvre, H. A simple optical technique to compensate for excess RIN in a fiber-optic gyroscope. In *2014 DGON Inertial Sensors and Systems (ISS)*, 1–14 (IEEE, 2014). https://doi.org/10.1109/InertialSensors.2014.7049411.

[21] Hotate, K. Resonator fiber optic gyro using digital serrodyne modulation: method to reduce the noise induced by the backscattering and closed-loop operation using digital signal processing. *Proc. SPIE* **3746**, 37463E (1999). https://doi.org/10.1117/12.2302112.

[22] Zheng, Y., Xu, H., Song, J., Li, L. & Zhang, C. Excess relative-intensity-noise reduction in a fiber optic gyroscope using a Faraday rotator mirror. *J. Light. Technol.* **38**, 6939–6947 (2020). https://doi.org/10.1109/JLT.2020.3020432.

[23] Algrain, M. C. & Ehlers, D. E. Novel Kalman filtering method for the suppression of gyroscope noise effects in pointing and tracking systems. *Proc. SPIE - Opt. Eng.* **34**, 3016–3030 (1995). https://doi.org/10.1117/12.210754.

[24] Narasimhappa, M., Sabat, S. L. & Nayak, J. Fiber-optic gyroscope signal denoising using an adaptive robust Kalman filter. *IEEE Sensors J.* **16**, 3711–3718 (2016). https://doi.org/10.1109/JSEN.2016.2535396.

[25] Noureldin, A., Irvine-Halliday, D., Tabler, H. & Mintchev, M. P. New technique for reducing the angle random walk at the output of fiber optic gyroscopes during alignment processes of inertial navigation systems. *Proc. SPIE - Opt. Eng.* **40**, 2097–2106 (2001). https://doi.org/10.1117/1.1404117.

[26] Qian, H. & Ma, J. Research on fiber optic gyro signal denoising based on wavelet packet soft-threshold. *J. Syst. Eng. Electron.* **20**, 607–612 (2009). https://ieeexplore.ieee.org/document/6074706.

[27] Zhu, R., Zhang, Y. & Bao, Q. A novel intelligent strategy for improving measurement precision of FOG. *IEEE Trans. Instrum. Meas.* **49**, 1183–1188 (2000). https://doi.org/10.1109/19.893253.

[28] Allan, D. W. Statistics of atomic frequency standards. *Proc. IEEE* **54**, 221–230 (1966). https://doi.org/10.1109/PROC.1966.4634.

[29] El-Sheimy, N., Hou, H. & Niu, X. Analysis and modeling of inertial sensors using Allan variance. *IEEE Trans. Instrum. Meas.* **57**, 140–149 (2008). https://doi.org/10.1109/TIM.2007.908635.

[30] Ng, L. C. On the application of Allan variance method for ring laser gyro performance characterization. Report, Lawrence Livermore National Laboratory (1993). https://www.osti.gov/biblio/10196087.

[31] IEEE. *IEEE Standard for Specifying and Testing Single-Axis Interferometric Fiber Optic Gyros* (2021). IEEE Std 952-2020 (Revision of IEEE Std 952-1997).

[32] Zheng, Y., Xu, H., Song, J., Li, L. & Zhang, C. Excess relative-intensity-noise reduction in a fiber optic gyroscope using a Faraday rotator mirror. *J. Light. Technol.* **38**, 6939–6947 (2020). https://doi.org/10.1109/JLT.2020.3020432.

[33] Yang, Y., Li, S., Yang, F. & Jin, W. Differential fiber optic gyroscope driven by two broadband sources of different wavelengths. *IEEE Access* **8**, 65443–65449 (2020). https://doi.org/10.1109/ACCESS.2020.2984006.

[34] Wheeler, J. M. & Digonnet, M. J. F. A low-drift laser-driven FOG suitable for trans-pacific inertial navigation. *J. Light. Technol.* **40**, 7464–7470 (2022). https://doi.org/10.1109/JLT.2022.3201189.

[35] Wang, L., Zhang, C., Lin, T., Li, X. & Wang, T. Characterization of a fiber optic gyroscope in a measurement while drilling system with the dynamic Allan variance. *Measurement* **75**, 263–272 (2015). https://doi.org/10.1016/j.measurement.2015.05.001.

[36] Freescale Semiconductor. *Allan Variance: Noise Analysis for Gyroscopes* (2015). AN5087, https://www.nxp.com/docs/en/application-note/AN5087.pdf.

[37] Jaroszewicz, L. R. *et al.* The fiber-optic rotational seismograph—laboratory tests and field application. *Sensors* **19** (2019). https://doi.org/10.3390/s19122699.

[38] Gundavarapu, S. *et al.* Interferometric optical gyroscope based on an integrated Si_3N_4 low-loss waveguide coil. *J. Light. Technol.* **36**, 1185–1191 (2018). https://doi.org/10.1109/JLT.2017.2765918.

[39] Kurzych, A. T., Jaroszewicz, L. R. & Kowalski, J. K. Development of three-axis fibre-optic seismograph for direct and autonomous monitoring of rotational events with perspective of historical review. *Sensors* **22** (2022). https://doi.org/10.3390/s22228902.

[40] Kamiński, M. *et al.* Firmware development for the fibre-optic seismometer based on FOG. *Opto-Electron. Rev.* **32**, 150179 (2024). https://doi.org/10.24425/opelre.2024.150179.

[41] Bernauer, F. *et al.* BlueSeis3A: Full characterization of a 3C broadband rotational seismometer. *Seismol. Res. Lett.* **89**, 620–629 (2018). https://doi.org/10.1785/0220170143.

[42] Bitline System. Mini broadband ASE light source. *oeMarket.com*. https://www.oemarket.com/catalog/product_info.php/mini-broadband-ase-light-source-p-50?osCsid=ca17da2751937df700d1726ef8757a5d (2024) (Accessed: 16th June 2024).

[43] Lloyd, S. W., Fan, S. & Digonnet, M. J. F. Experimental observation of low noise and low drift in a laser-driven fiber optic gyroscope. *J. Light. Technol.* **31**, 2079–2085 (2013). https://doi.org/10.1109/JLT.2013.2261285.